AGU PUBLICATIONS

JGR

Journal of Geophysical Research: Solid Earth

RESEARCH ARTICLE

10.1002/2015JB012408

**Key Points:**

- A 3-D model of seismic *P* wave anisotropy beneath Taiwan is presented
- The anisotropy in the crust delineates geological structures in eastern Taiwan
- Anisotropy reveals collision-induced displacements below the crust of Taiwan

**Correspondence to:**
I. Koulakov,
KoulakovIY@ipgg.sbras.ru

**Citation:**
Koulakov, I., A. Jakovlev, Y.-M. Wu, N. L. Dobretsov, S. El Khrepy, and N. Al-Arifi (2015), Three-dimensional seismic anisotropy in the crust and uppermost mantle beneath the Taiwan area revealed by passive source tomography, *J. Geophys. Res. Solid Earth*, *120*, 7814–7829, doi:10.1002/2015JB012408.

Received 1 AUG 2015
Accepted 27 OCT 2015
Accepted article online 31 OCT 2015
Published online 26 NOV 2015



# Three-dimensional seismic anisotropy in the crust and uppermost mantle beneath the Taiwan area revealed by passive source tomography

**Ivan Koulakov[1,2], Andrey Jakovlev[1,2], Yih-Min Wu[3,4], Nikolay L. Dobretsov[1,2], Sami El Khrepy[5,6], and Nassir Al-Arifi[5]**

[1]Trofimuk Institute of Petroleum Geology and Geophysics, SB RAS, Novosibirsk, Russia, [2]Department of Geology and Geophysics, Novosibirsk State University, Novosibirsk, Russia, [3]Department of Geosciences, National Taiwan University, Taipei, Taiwan, [4]National Center for Research on Earthquake Engineering, Taipei, Taiwan, [5]Department of Sciences, King Saud University, Riyadh, Saudi Arabia, [6]National Research Institute of Astronomy and Geophysics, Helwan, Egypt

**Abstract** We present a 3-D anisotropic seismic model of the crust and uppermost mantle beneath the Taiwan region based on the tomographic inversion of traveltime data from regional earthquakes. In the crust beneath eastern Taiwan, we observe coast-parallel anisotropy that perfectly delineates the major geological structures. In westernmost Taiwan, we distinguish a crustal block corresponding to the Peikang High at the margin of the Eurasian Plate, where coast-perpendicular anisotropy within a high-velocity anomaly is observed. In the uppermost mantle, the direction of anisotropy beneath central Taiwan turns perpendicular to the coast, which may indicate eastward underthrusting of the Peikang Block that was induced by collisional processes. To the NE of Taiwan, the anisotropy forms circular patterns coinciding with the shape of the Ryukyu arc, which may reflect the distribution of the deformations and fractures in the accretion and arc complex.

## 1. Introduction

Taiwan is a singular point on the world tectonic map at which the Philippine Sea Plate (PSP) collides with the Eurasian Plate (EAP) in two subduction zones with nearly opposite orientations [e.g., *Suppe*, 1984; *Teng*, 1990; *Koulakov et al.*, 2014], where intensive collisional processes are concentrated in a relatively small area. This collision created sharp topography contrasts (Figure 1a) and complex geological structures (Figure 1b). The causes of such a concentration of tectonic processes are discussed in many studies [*Suppe*, 1984; *Wu et al.*, 1997, 2007; *Ustaszewski et al.*, 2012; *Kuo-Chen et al.*, 2012; *Huang et al.*, 2014a, 2014b]. *Huang et al.* [2014b] reported tomography images at the Ryukyu-Manila trench junction of Taiwan, which displays flipping subductions. However, the details regarding the crustal and uppermost mantle deformations beneath Taiwan Island are still far from completely understood. Large amounts of onshore seismic stations and intensive seismic activity in the area provide rich information for studying high-resolution structures beneath Taiwan and the surrounding areas. Traveltimes from passive source observations recorded by permanent and temporary stations in Taiwan were used to compute several high-resolution seismic models of the crust and upper mantle [e.g., *Wang et al.*, 2006; *Hsu*, 2001; *Kim et al.*, 2005; *Lin et al.*, 2007; *Wu et al.*, 2007, 2009; *Ku and Hsu*, 2009; *Kuo-Chen et al.*, 2012; *Koulakov et al.*, 2014]. Surface wave and ambient noise tomography schemes are also implemented to study the deep structures [e.g., *Hwang and Yu*, 2005; *You et al.*, 2010; *Huang et al.*, 2012] but not as intensively as with the use of the body wave data.

Anisotropy is an important additional parameter that provides information on the characteristics of the dynamic processes in the crust and upper mantle. For example, azimuthal anisotropy can be connected with the major faulting and thrusting in the crust that, in turn, represents the distribution of regional stresses and deformations. For the upper mantle, azimuthal anisotropy may be caused by the predominant orientations of olivine crystals, which may indicate the direction of mantle displacement (e.g., see overview in *Long* [2013]). Anisotropy studies have been performed in different subduction zones, such as the Izu-Bonin arc [*Anglin and Fouch*, 2005], New Zealand [e.g., *Audoine et al.*, 2004], the Aleutian-Alaska arc [e.g., *Yang et al.*, 1995], Ryukyu arc [*Long and Van der Hilst*, 2006], Hokkaido [e.g., *Koulakov et al.*, 2015], and Kamchatka [*Levin et al.*, 2004]. These and other anisotropy studies have helped to reveal important constraints on the general mechanisms of tectonic processes.

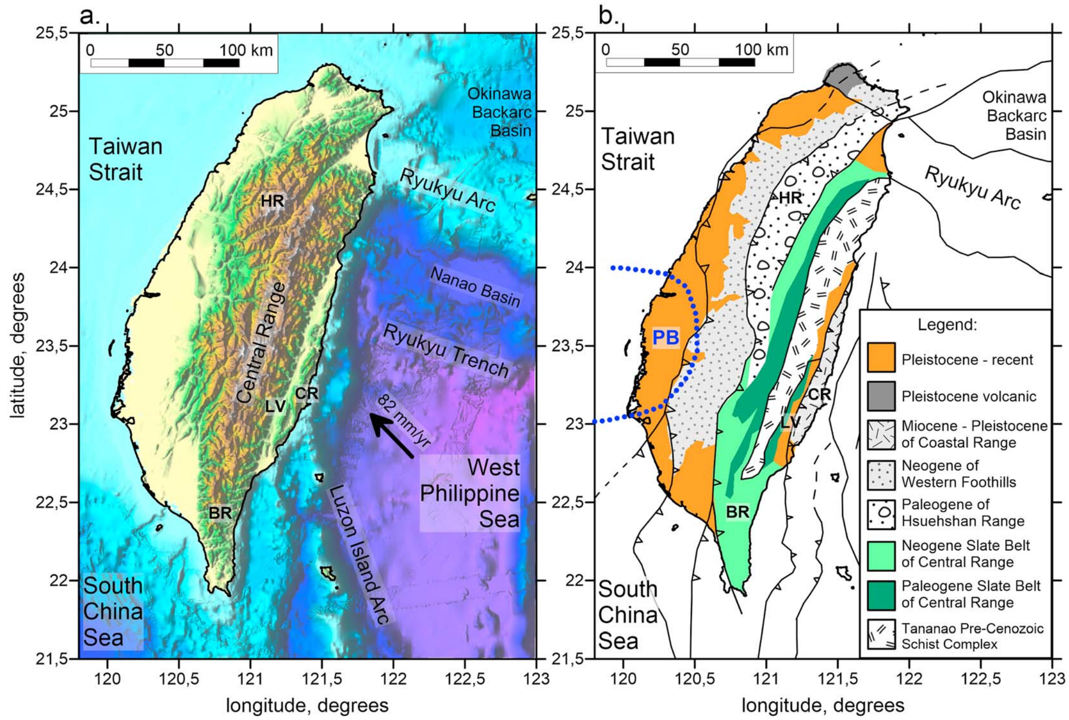


**Figure 1.** (a) Topography/bathymetry in the Taiwan region with indications of the major geological and tectonic units. (b) Simplified geological scheme of the onshore areas of Taiwan (modified from *Huang et al.* [2006] and *Chen et al.* [2003]). Blue dotted line with PB indicates Peikang Block. HR is Hsueshan Range, CR is Coastal Range, LV is Longitudinal Valley, and BR is Backbone Range.

In the Taiwan region, anisotropy has been studied based on shear wave splitting methods and tomography inversions. For example, *Rau et al.* [2000] performed the splitting analysis of teleseismic *S* waves and obtained coherent patterns in most stations, indicating an SN orientation for the anisotropy. Based on a good fit for the observed anisotropy with the major lineaments on the surface (faults, ridges, and elongated geological structures), the authors proposed that the observed strong anisotropy is caused by crustal structures. Note, however, that teleseismic data splitting cannot provide exact information on the depth of the anisotropic layer. Similar anisotropy patterns were identified by *Huang et al.* [2006] using teleseismic *S* wave data recorded by stations along the profile in central Taiwan. The splitting information from local and regional events allows us to determine the location of the anisotropic zone more precisely. For example, *Chang et al.* [2009] analyzed shear wave splitting corresponding to regional earthquake data and identified clear anisotropy patterns that are attributed to the crust. More complex anisotropy structure follows from the analysis of the group and phase velocities of surface waves derived from ambient noise correlation in a recent study by *Huang et al.* [2015]. These authors found clear SN oriented anisotropy in the upper crust and almost perpendicular orientations below 10 km depth. Based on these results, they proposed a layered mechanism of deformation in the Taiwan orogeny with almost independent processes below and above the 10 km level. These anisotropy observations are supported by several active and passive body wave tomography studies. For the Taiwan region, there is a unique opportunity to use high-quality active source data collected within the TAIGER explosion experiment. *Kuo-Chen et al.* [2013] used these data to study *P* wave anisotropy in the upper crust and found that the fast velocities are generally oriented NNE along the main tectonic structures in Taiwan. Passive source traveltime observations were also used to identify the anisotropic structure in Taiwan. In particular, *Chen et al.* [2003] performed tomography studies for *Pn* waves and obtained clear coast-perpendicular orientation for anisotropy just below the crust. This seems to be consistent with the results of *Huang et al.* [2015], who found a switch in the anisotropy patterns from coast parallel in the crust to coast perpendicular in the uppermost mantle. These and other studies show that the anisotropy structure beneath Taiwan is fairly complicated, and the inconsistencies between different models appear to be quite important. These misfits can be due to the different sensitivities and resolution capacities of various methods

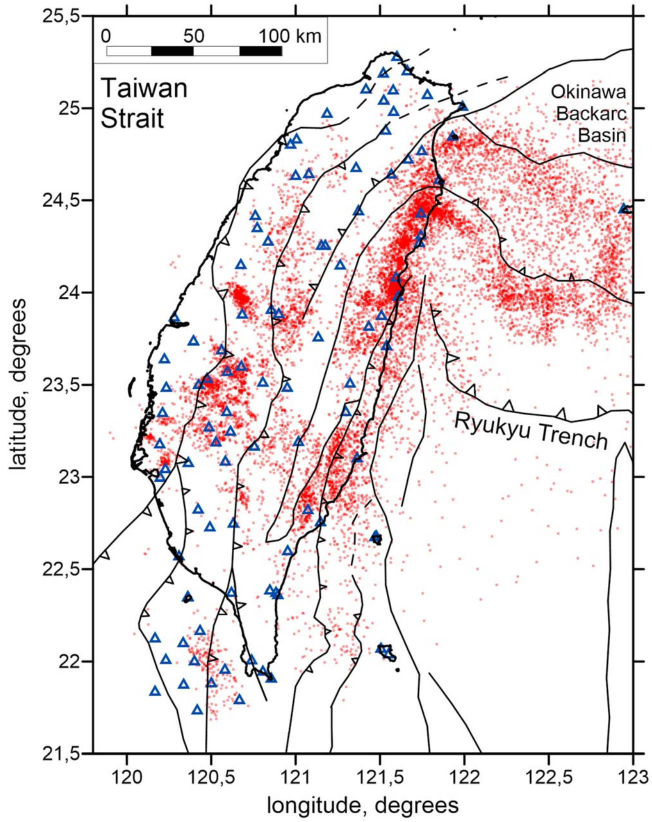


**Figure 2.** The distribution of data used in this study: blue triangles are the stations; red dots are the earthquakes. Major geological structures are highlighted according to Figure 1.

and possibly different behaviors of *P* and *S* waves in anisotropic media. This shows that the problem of anisotropy determination is far from a final resolution, and any independent anisotropy studies give more constraints on the real underground structure.

In this study, we present a new 3-D distribution model of the *P* velocity anisotropy beneath the Taiwan region based on the algorithm of passive source anisotropic tomography ANITA and the traveltime data of regional seismological networks.

## 2. Data and Algorithm

For this study, we use data from a comprehensive data set of Taiwanese catalogues. The data set combined several seismic networks [*Wu et al.*, 2007, 2008, 2009], including the Taiwan Central Weather Bureau Seismic Network (CWBSN), Japan Meteorological Agency (JMA), and some temporal Ocean Bottom Seismometer stations deployed by the National Central University (NCU). In total, we used data from 115 seismic stations in the Taiwan area, which are shown in Figure 2. Anisotropic tomography inversion requires denser coverage and higher data quality than regular isotropic inversion. Therefore, we only used relatively strong events with more than 30 recorded *P* and *S* phases for the inversion. To be selected, the events should be located at a distance of less than 200 km from the nearest station. Note that some of the events were located outside the network perimeter that should worsen the accuracy of their locations. At the same time, as was shown by *Koulakov* [2009a], adding out-of-network events improves the ray coverage beneath stations, increases the number of data, and thus enhances the resolution of the tomography model. Although the mislocations for such remote events might be significant, they do not have a crucial effect upon the tomography results. In these cases, the most important are relative residuals recorded by different stations that provide the information about anomalies beneath the network. This statement was supported by synthetic tests in *Koulakov* [2009a] with the data configuration similar to that used in this study.

To reject the outliers, we used the thresholds of 1 s and 1.5 s for the *P* and *S* residuals, respectively, computed after the step of source locations in the starting 1-D model. As a result, for the tomography, we selected 4243 events with a total number of 141,979 *P* and 74,828 *S* phases. The distributions of the stations and events used in this study are shown in Figure 2.

Here we use a passive source tomography algorithm, ANITA, developed by *Koulakov et al.* [2009], which was previously implemented to study crustal and uppermost mantle anisotropic structures beneath Central Java [*Koulakov et al.*, 2009], Central America [*Rabbel et al.*, 2011], and Hokkaido [*Koulakov et al.*, 2015]. The most recent version of the algorithm, same as used in this study, is described in details in *Koulakov et al.* [2015]. This algorithm is based on a general concept of the LOTOS code [*Koulakov*, 2009b], which performs the simultaneous iterative inversion of passive source data for *P* and *S* velocity structures and source parameters. In the present version of the ANITA code, the azimuthal anisotropy is only derived for the *P* velocity model. For the *S* model, anisotropic parameterization was not implemented because standard data catalogues do

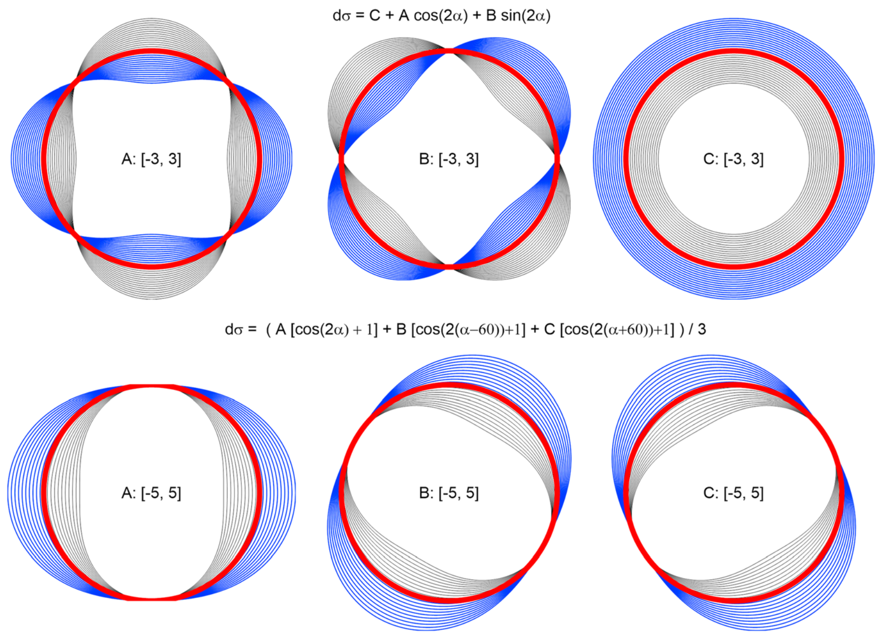


**Figure 3.** Two types of the azimuthal anisotropy parameterization. (top row) Traditional parameterization from *Hearn* [1996] and (bottom row) parameterization from *Koulakov et al.* [2009], which is used in this study. Deviations of each parameter are given inside the circles; blue lines depict positive deviations of the corresponding parameter, and red circle is the reference level.

not contain information on split "fast" and "slow" shear waves, which should be considered when *S* velocity anisotropy is studied. This version of the ANITA code is based on node parameterization (same as in the LOTOS code) and not cell parameterization, as used in older versions.

Here we study the azimuthal anisotropy with orthogonal orientations of slow and fast velocities in horizontal plane. In each point of the three-dimensional space, such anisotropy can be represented by three parameters: minimum and maximum velocities and the azimuth of the fast velocity orientation. Unfortunately, the angle cannot be used as a parameter in the linearized tomographic problem; therefore, in tomography schemes, the anisotropy is usually parametrized by three other parameters. For example, in most previous studies, the azimuthal anisotropic model is approximated using a formula proposed by *Hearn* [1996]:

$$\mathrm{d}\sigma = C + A\cos 2a + B\sin 2a, \tag{1}$$

where $\alpha$ is azimuth of the ray propagation, *A* and *B* represent the anisotropy deviations along 0 and 45°, and *C* is the isotropic variation of slowness. The anisotropy indicatrices corresponding to deviations of each of these three coefficients are shown in Figure 3 (top row).

In this study, we implement the parameterization proposed by *Koulakov et al.* [2009] that uses three parameters corresponding to three predefined directions along 0°, 60°, and 120°, as shown in Figure 3 (bottom row). The slowness deviation is the horizontal plane that can be represented as

$$\mathrm{d}\sigma_{\mathrm{hor}} = \{A[\cos 2a + 1] + B[\cos(2(a-60)) + 1] + C[\cos(2(a+60)) + 1]\}/3, \tag{2}$$

where *A*, *B*, and *C* are the slowness deviations along the azimuths of 0°, 60°, and 120°. In the three-dimensional case, the slowness along a ray, with the azimuth, $\alpha$, and dip angle, $\beta$, (measured upward from the vertical axis) can be represented as follows:

$$\sigma = \sigma_{\mathrm{ref}} + (\mathrm{d}\sigma_{\mathrm{hor}}\sin\beta + \mathrm{d}\sigma_{\mathrm{ver}}\cos\beta)/(\sin\beta + \cos\beta), \tag{3}$$

where

$$\mathrm{d}\sigma_{\mathrm{ver}} = (A + B + C)/3, \tag{4}$$

and $\sigma_{\mathrm{ref}}$ is reference slowness value. This parameterization represents a pseudoellipse with the orthogonally oriented maximum and minimum values of slowness ($\mathrm{d}\sigma_{\mathrm{max}}$ and $\mathrm{d}\sigma_{\mathrm{min}}$) and azimuth of maximum slowness orientation ($\psi$). The parameters $A$, $B$, and $C$ can be uniquely converted to $d\sigma_{max}$, $d\sigma_{min}$, and $\psi$ and vice versa. Examples of the azimuthal anisotropy representation using this parameterization are shown in Figure 3.

We prefer using the formula (2) rather than (1) for approximation of the anisotropy because it uses absolutely equivalent parameters, whereas in formula (1), the parameters responsible for the isotropic ($C$) and anisotropic parts are different in their nature. This may cause some ambiguity when assigning weights during inversion. In the case of using formula (2), all parameters describing the anisotropy are absolutely equivalent. Although the parameters $A$, $B$, and $C$ in formula (2) are formally not independent, in practice, the basic orientations spaced at 60° provide fair approximations of anisotropy, as will be shown by synthetic tests. Finally, this parameterization is more convenient for modeling as directly representing velocity values in each of three orientations.

In this version, we do not consider an independent parameter describing the variation in vertical anisotropy because it appeared to be unstable and strongly dependent on the choice of free inversion parameters in most cases of local earthquake tomography.

The traveltime along the seismic ray is computed as integral along a path between source and receiver:

$$T = \int_{\text{path}} \sigma(\alpha(s), \beta(s)) \mathrm{d}s, \tag{5}$$

where the slowness $\sigma$ is computed according to formulas (1) and (2) according to azimuth $\alpha$ and incidence angle $\beta$ in a current point $s$. We solve a linearized problem for slowness variations, $\Delta\sigma$, as the model parameters, and time residuals, $\Delta t$, in the data vector. In addition, we consider the effect of source mislocation, $\Delta h$, and origin time shift, $\Delta t_0$. As a result, equation (3) is reduced to

$$\Delta t = \int_{\text{path}} \Delta\sigma(\alpha(s), \beta(s)) \mathrm{d}s + \sum_{m=1}^{3} P_m \Delta h_m + \Delta t_0, \tag{6}$$

where $P_m$ is the slowness vector (ray orientations) in the source point.

The 3-D anisotropic distribution of the $P$ velocity anisotropy is parameterized using a set of nodes distributed in the study volume according to the ray density similarly as in the isotropic version of the LOTOS code [*Koulakov*, 2009b]. Between the nodes, the slowness parameters are interpolated using the three-linear interpolation. The discrete parameterization reduces the integral representation (4) to the system of linear equations:

$$\Delta t_i = \sum_{j=1}^{N} \sum_{k=1}^{K} A_{ijk} \Delta\sigma_{jk} + \sum_{m=1}^{3} P_m \Delta h_m + \Delta t_0, \tag{7}$$

where $i$ is the number of the ray, $j$ is the number of the parameterization cell, $k$ is the number of the anisotropic orientations (0, 60, or 120°) in the case of anisotropic $P$ model and 1 for the isotropic $S$ model, and $A_{ijk}$ is the first-derivative matrix representing the traveltime variation due to unit change of slowness in the $j$th cell corresponding to the $k$th orientation. This matrix is computed numerically along the raypath derived from the previous location step using formulas (2) and (3).

The amplitude and flattening of the model, as well as the anisotropy strength, are controlled by additional matrix blocks. The amplitudes of anomalies are tuned by a diagonal matrix corresponding to a system of trivial equations:

$$D^{\text{amp}} \Delta\sigma_{jk} = 0, \tag{8}$$

where $D^{\text{amp}}$ is the amplitude damping coefficient.

To flatten the anomalies in space, we used another matrix block, which minimizes the differences of slowness anomalies in neighboring nodes and can be represented by the equations

$$D^{sm} \left( \Delta\sigma_{j1,k} - \Delta\sigma_{j2,k} \right) = 0, \tag{9}$$

where $j1$ and $j2$ represent parameters in neighboring nodes corresponding to the same orientation of anisotropy, $k$; $D^{sm}$ is the smoothing coefficient. This block includes all combinations of neighboring nodes in the grid for the three azimuths of 0, 60°, and 120°.

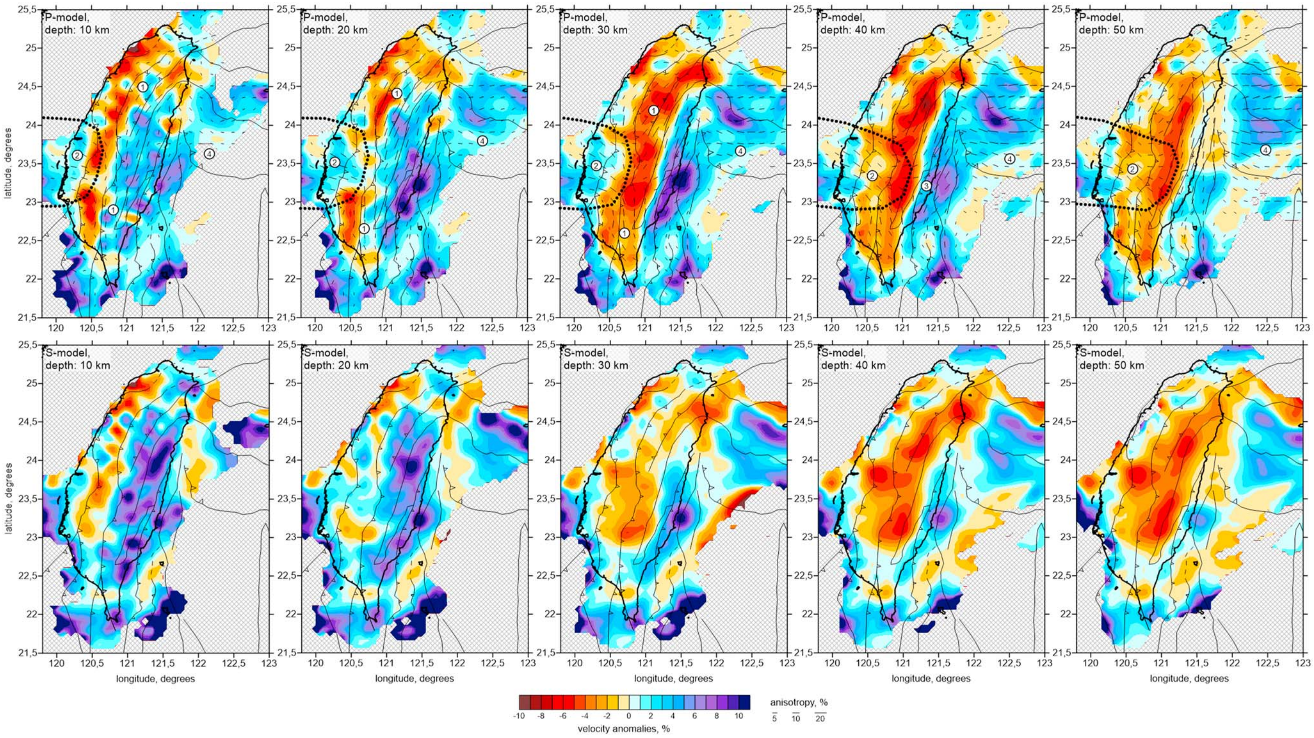


**Figure 4.** Anisotropic *P* and isotropic *S* wave velocity models presented in five horizontal sections. The orientations of fast velocities in the *P* model are indicated with bars. Numbers indicate the main structures discussed in the text. Dotted lines highlight an area with coast-perpendicular anisotropy interpreted as the Peikang Block underthrusted underneath Taiwan. Major geological structures are highlighted according to Figure 1.

Finally, the anisotropy strength is controlled by minimizing the differences of slowness anomalies in the same node along different azimuths:

$$D^{\mathrm{anis}}\left(\Delta\sigma_{j,k1} - \Delta\sigma_{j,k2}\right) = 0, \tag{10}$$

where $D^{\mathrm{anis}}$ is the parameter of anisotropy damping and $\Delta\sigma_{j,k1}$ and $\Delta\sigma_{j,k2}$ are the slowness anomalies in different directions at the same node.

The inversion of the matrix is performed by using the damped LSQR method [*Paige and Saunders*, 1982; *Nolet*, 1987].

Each iteration of tomography processing in ANITA starts with the source locations in the updated 3-D anisotropic model. The traveltimes for the *P* and *S* rays are computed by the bending method, presuming that the raypath deformations achieve the minimum traveltime taking into account azimuthal differences of velocity in the 3-D anisotropic velocity model. When constructing the raypath, both source and receiver may have arbitrary depth/elevation coordinates. The locations of the sources are determined by searching for the goal function's maximum, as described in *Koulakov and Sobolev* [2006]. A parameterization mesh is constructed taking into account the ray distributions. To avoid any effects related to the grid configuration, we perform the inversions for several parameterization grids with different basic azimuthal orientations (0, 22, 45, and 67°). The grids are only constructed in the first iteration; in the following iterations, velocity anomalies are updated in the same nodes. In our case, we defined 5 km as the minimum grid spacing in the horizontal and vertical directions. The total amount of nodes for the *P* and *S* models in each of the four grids was approximately 16,600 and 14,500, respectively. The matrix calculation and inversion stages are performed separately and consecutively for the isotropic and anisotropic models. The details of the anisotropic model parameterization are presented above. For the isotropic case, computing the first-derivative matrix and inversion is performed similarly to the LOTOS code [*Koulakov*, 2009b]. After the isotropic inversion, the data are updated by subtracting the residuals computed in the previously obtained isotropic velocity variation model. The anisotropic inversion is conducted for the *P* model. The isotropic *S* model and the source parameters are updated simultaneously during the anisotropic inversion.

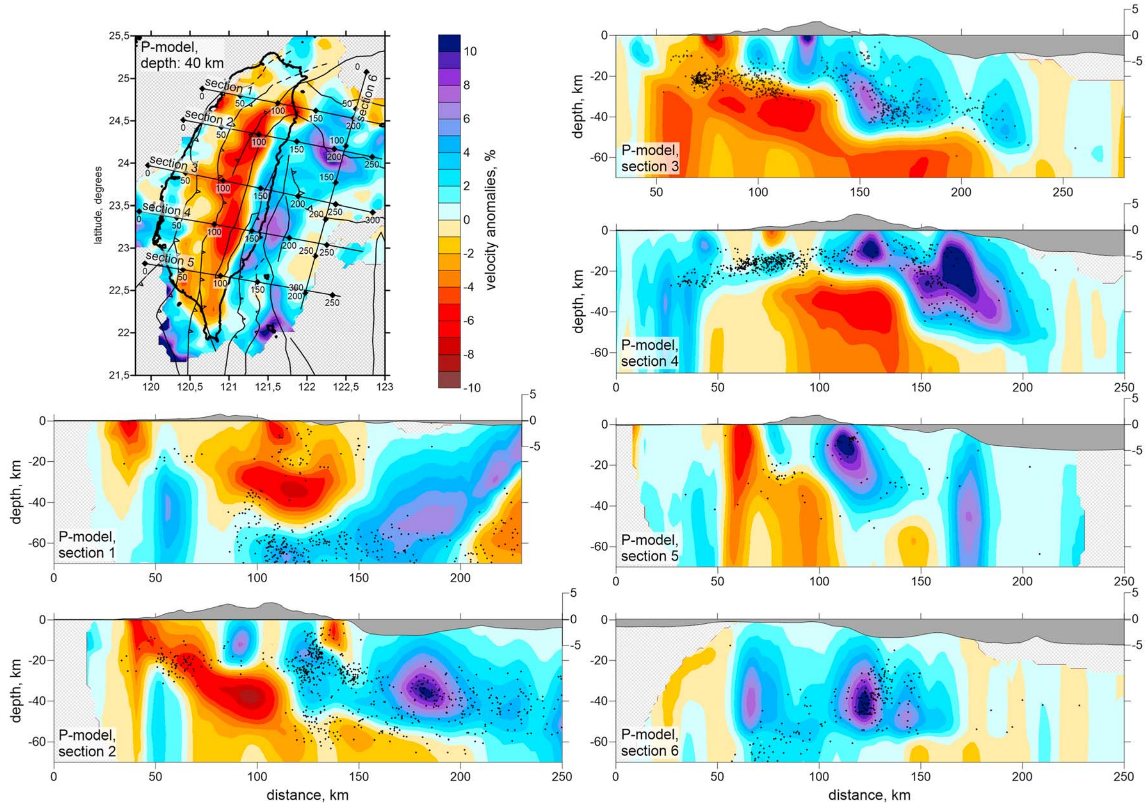

**Figure 5.** *P* velocity anomalies presented in six vertical sections. Locations of the sections are shown in the map. Dots indicate the projections of earthquakes at distances of less than 15 km from the profile. Exaggerated relief is shown above each profile.

The values of the regularization parameters and the weights of the source parameters are determined based on the results of synthetic modeling. When performing synthetic tests, we simulate the calculation conditions as close as possible to the case of the observed data inversion. We tune the inversion coefficients to achieve the maximal resemblance of the original synthetic model with the reconstruction results and then use their values for the experimental data inversion. Details of the synthetic modeling are presented in the next section.

## 3. Inversion Results

The main results of this study, the anisotropic *P* and isotropic *S* velocity models, were obtained after three inversion iterations. Figure 4 presents *P* and *S* velocity anomalies in horizontal sections. For the *P* velocity model, bars indicate orientations of fast velocities. Vertical sections of the resulting *P* and *S* anomalies are shown in Figures 5 and 6. Absolute *P* and *S* velocities are presented in vertical sections in Figures 7 and 8. Since we use the azimuthal parameterization for anisotropy, no information on the anisotropic parameters is presented in vertical sections. Comparing the *P* and *S* velocity models demonstrates rather good correlation. It can be seen that the isotropic anomalies generally correspond to the previous seismic models by *Wu et al*. [2007], *Kuo-Chen et al*. [2012], and *Huang et al*. [2014a]. The shallower part is generally consistent with the ambient noise tomography results of *Huang et al*. [2012], but in deeper sections, these models look considerably different, probably due to the different depth resolutions of these two methods. Before discussing the interpretation of these models, we will present several tests aiming at assessing the robustness of the results.

The workflow of the ANITA code allows us to remove the anisotropic inversion step, which reduces the processing to purely isotropic inversion. To estimate the role of the anisotropic parameters, we compared the variance reduction values for the isotropic and anisotropic inversions. After three iterations, the reduction of the *P* residuals was only 20.6% for the isotropic model and 33.3% for the anisotropic model.

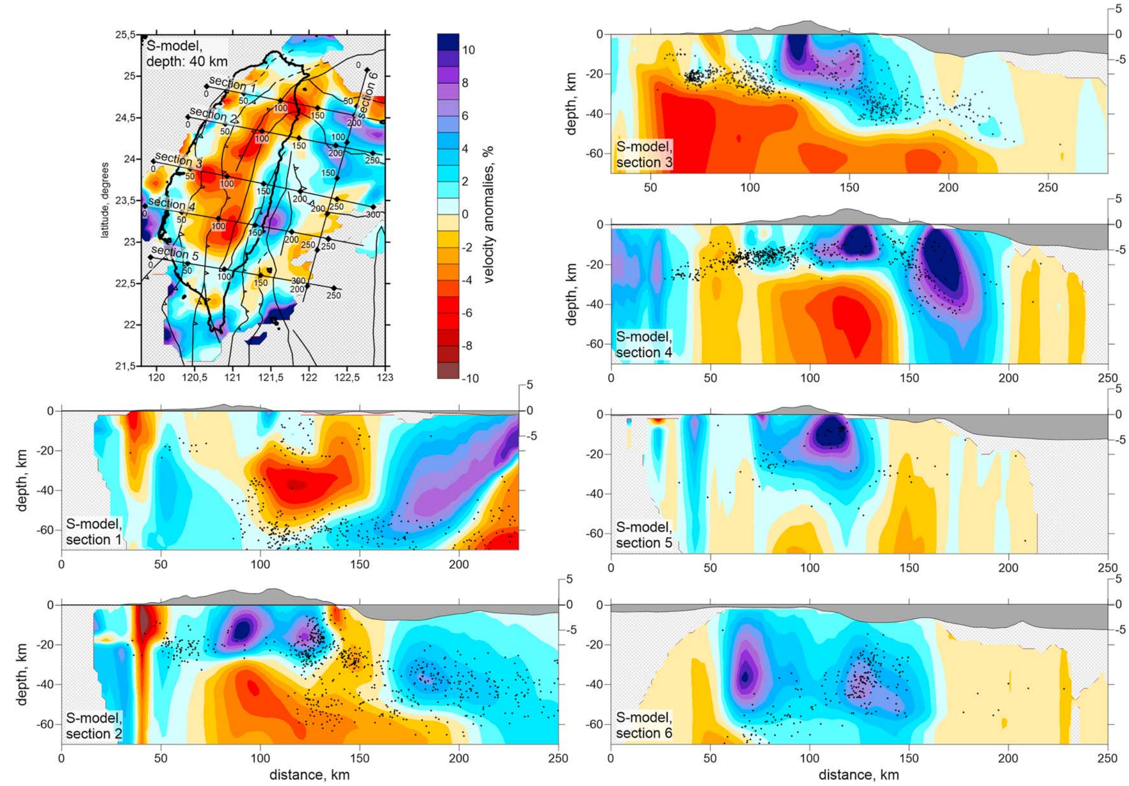


**Figure 6.** Same as Figure 4 but for the *S* model.

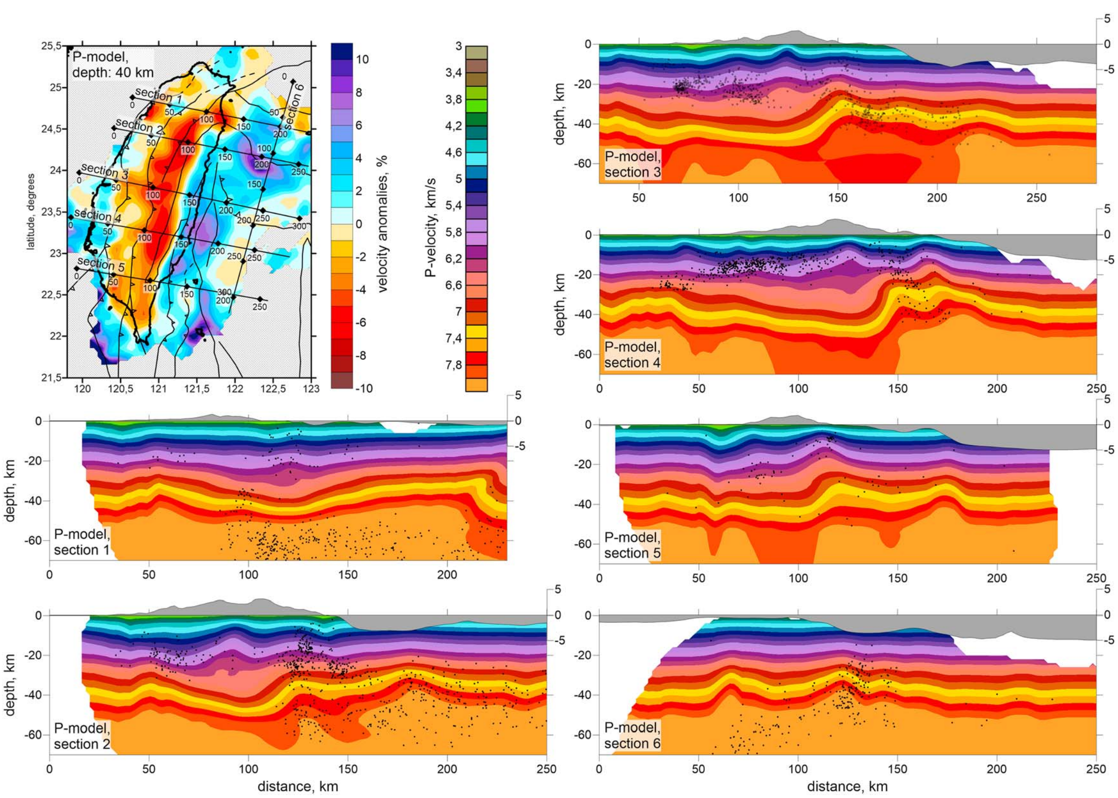


**Figure 7.** Absolute *P* velocity presented in six vertical sections. Locations of the sections are shown in the map with velocity anomalies. Dots indicate the projections of earthquakes at distances of less than 15 km from the profile. Exaggerated relief is shown above each profile.

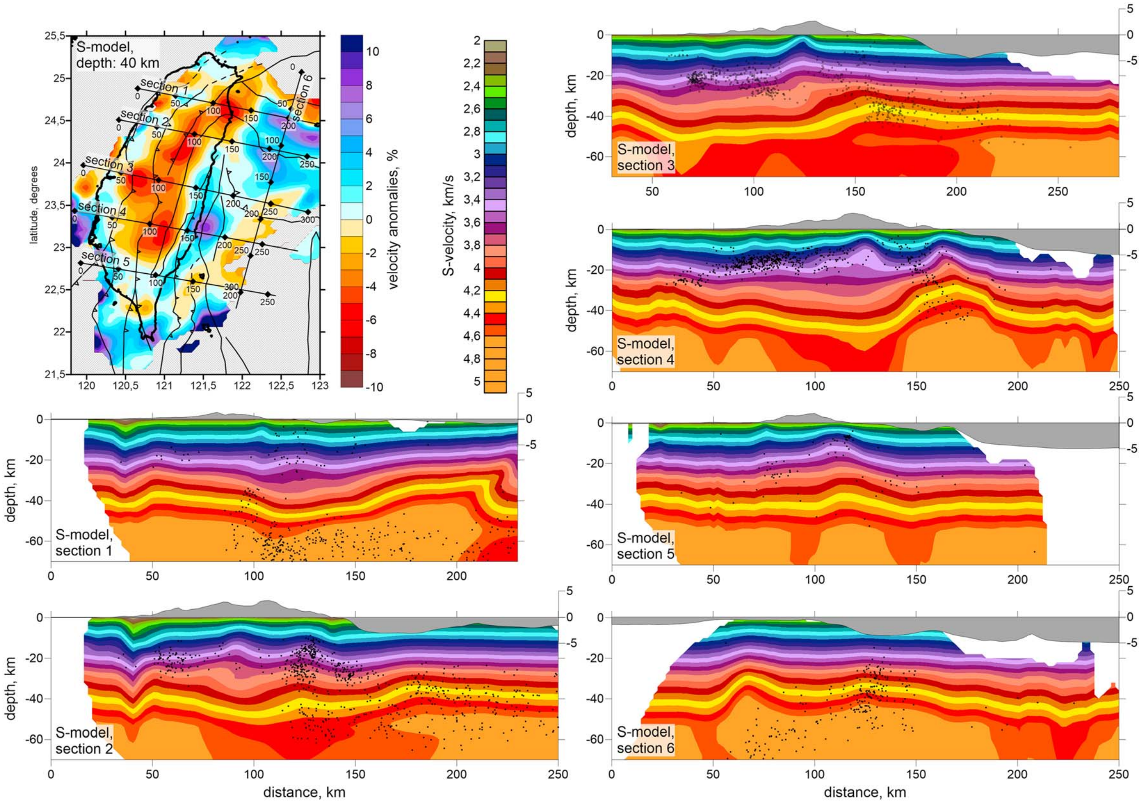


**Figure 8.** Same as Figure 6 but for the *S* velocity.

When comparing the locations in the starting 1-D model and final 3-D anisotropic model, the residuals of the *P* data reduced from 0.622 s to 0.414 s, and those of the *S* data reduced from 1.043 s to 0.663. Larger reduction for the *S* wave residuals is because they are more sensitive to velocity anomalies (same values of velocity anomalies provide larger residuals of the *S* data compared to that of *P*).

The result of the isotropic inversion is presented in Figure 9. The *P* anomalies in the isotropic and anisotropic models look almost identical at shallow depths, whereas the isotropic model provides much smoother anomalies in deeper sections. The observed difference between the isotropic and anisotropic inversions is partly due to an additional increase of anomalies in the isotropic model caused by the anisotropic inversion. However, we estimate that the major part of the difference in the variance reduction is due to the anisotropic effect, which appears to be relatively strong for Taiwan. Here we observe approximately 16% improvement in the data fit due to the anisotropic factor, whereas this reduction was much weaker in other previously studied areas (~10% in Central Java [*Koulakov et al*., 2009] and 4–8% in Central America [*Rabbel et al*., 2011]). This clearly indicates the strong value of anisotropy in the Taiwan area, which should be taken into account during the inversion.

The spatial resolution of the isotropic and anisotropic parameters can be assessed by synthetic modeling. In Figures 10 and 11, we present the results of three checkerboard tests for the anisotropic *P* and isotropic *S* wave velocity model with different lateral sizes of synthetic anomalies: 75, 50, and 35 km. The values of isotropic anomalies for the *P* and *S* models are ±5%. The anisotropy for the *P* model was defined by 5% difference of velocities in two orthogonal directions. In the low-velocity (red) patterns, the fast velocity orientation was longitudinal; for the high-velocity patterns (blue), it was latitudinally oriented. The signs of anomalies and orientations of anisotropy change at 30 km depth. The synthetic traveltimes were computed in the anisotropic model by the bending method of ray tracing. Additionally, the synthetic traveltimes were perturbed with random noise with the average deviations of 0.2 s for both *P* and *S* data. This level of noise provided similar values of average deviations of remnant residuals after inversions as in the case of observed

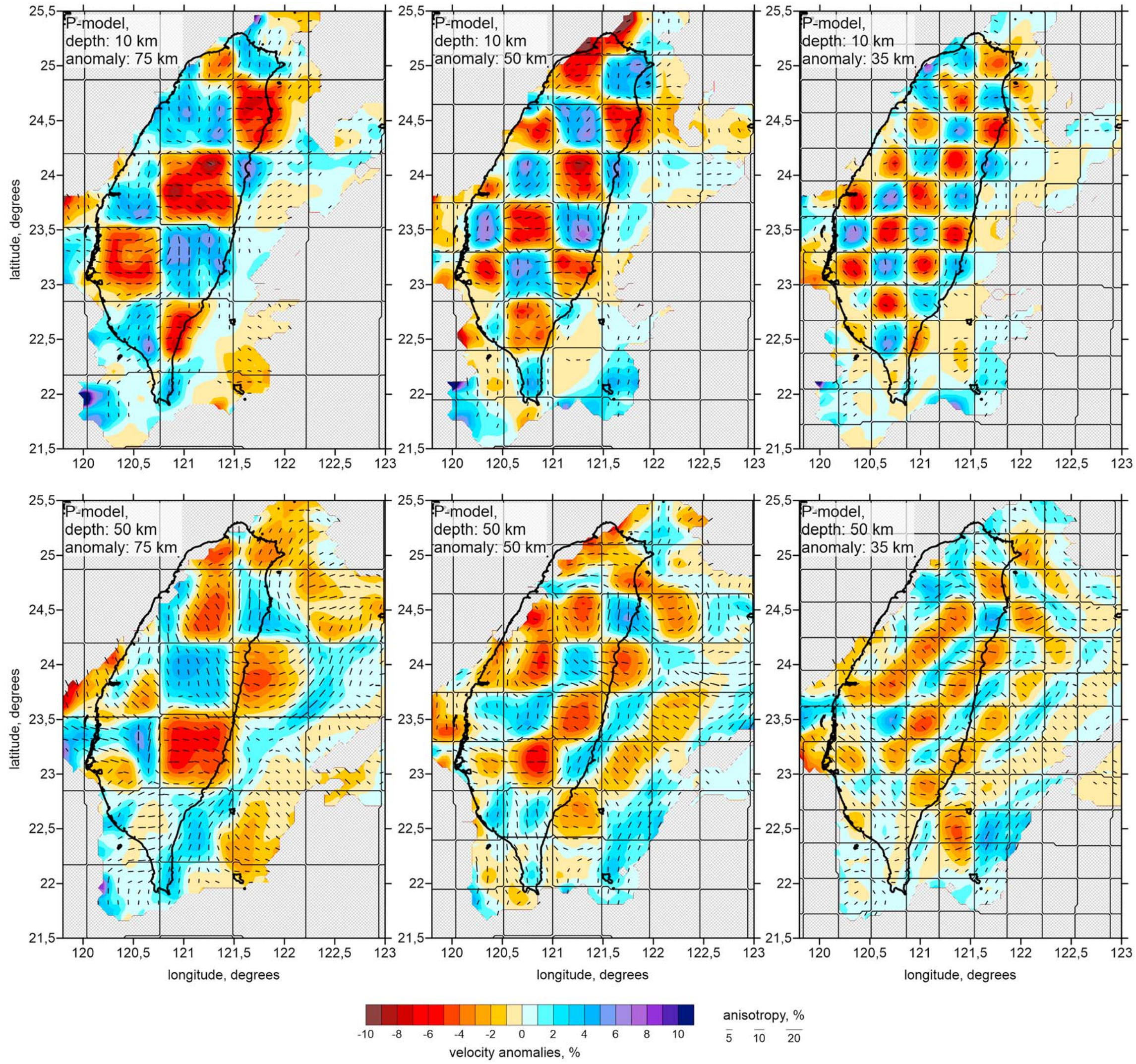


**Figure 9.** Checkerboard test for three anisotropic *P* wave velocity models. The shapes of the synthetic anomalies are shown with thin black contours. For the anisotropic model, in the negative (red) patterns, the anisotropy is oriented latitudinally; in positive (blue) patterns it is longitudinally oriented. The change of the sign of anomalies and anisotropy orientations occurs at 30 km depth. Sizes of anomalies are 75, 50, and 35 km.

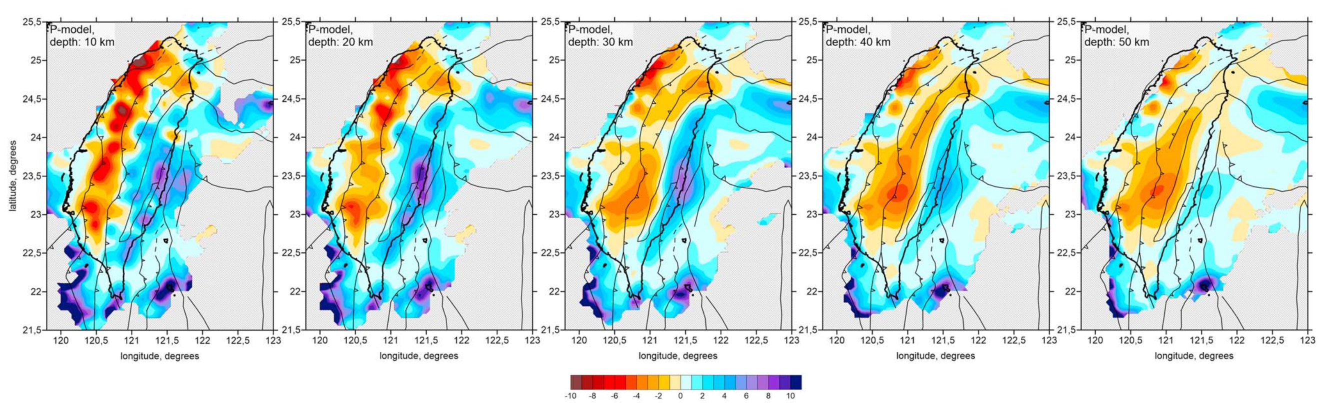


**Figure 10.** Result of isotropic inversion for the *P* velocity model. Major geological structures are highlighted according to Figure 1.

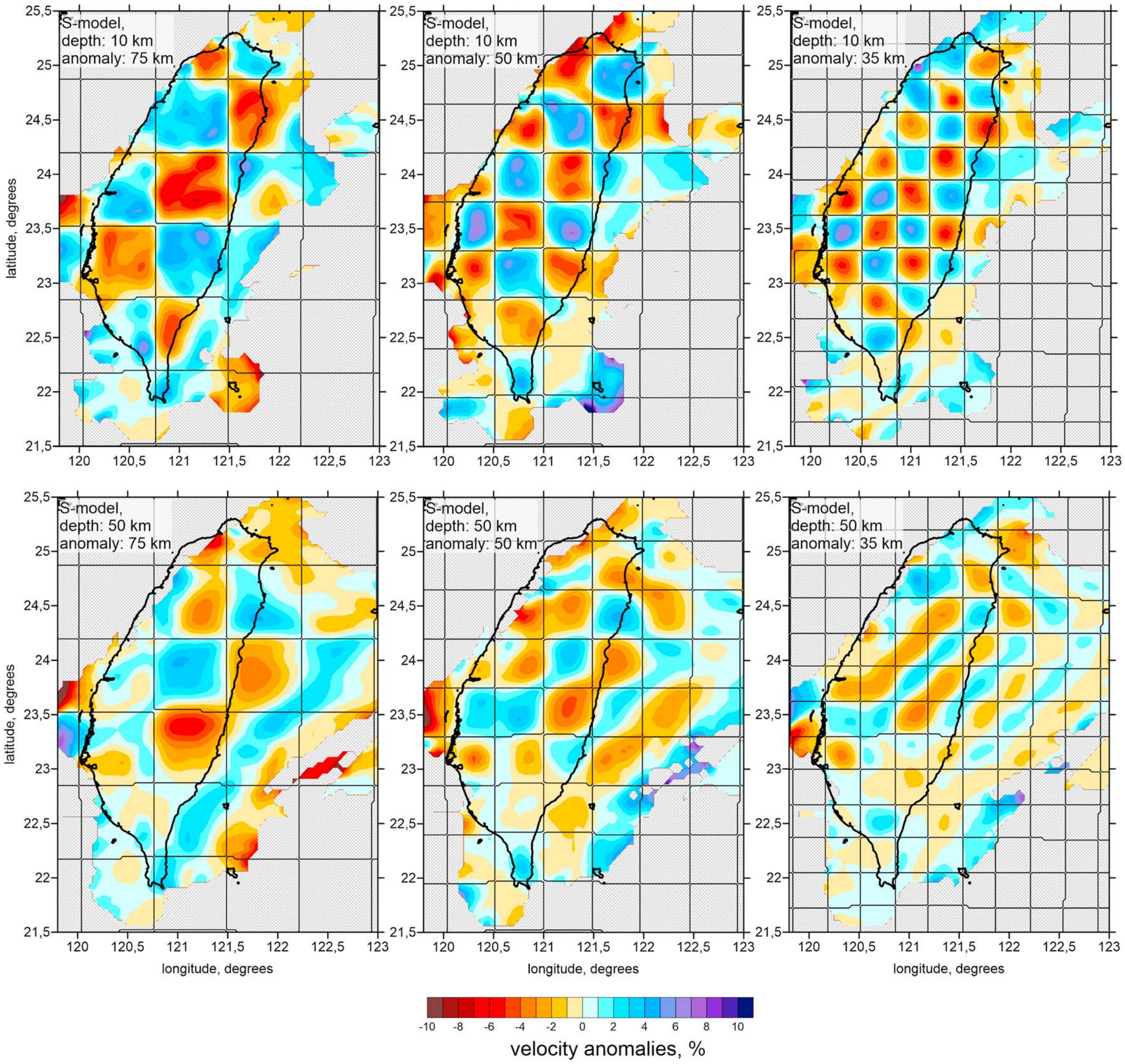


**Figure 11.** Checkerboard test for three isotropic *S* wave velocity models. The shapes of the synthetic anomalies are shown with thin black contours. The change of the sign of anomalies occurs at 30 km depth. Sizes of anomalies are 75, 50, and 35 km.

data analysis (0.35–0.40 s). Before starting the reconstruction, we "forget" the information on the sources and run the full inversion procedure, same as used in the case of real data analysis. We used same values of the inversion parameters, as in the case of computing the main model. For both *P* and *S* models, we obtain rather good reconstruction of the main patterns in the onshore areas for all models in the upper layer. In the lower layer, the robust reconstruction is observed for anomalies of 75 and 50 km size. For the 35 km size anomalies we see some smearing showing the resolution limitations at this depth. The anisotropic parameters in the *P* model (Figure 10) appear to be less stable. The correct orientations of anisotropy are only restored in central parts of the anomalies. In the case of 35 km size of anomaly, the anisotropy patterns could not be reconstructed. These tests give the confident size of the isotropic and anisotropic anomalies that can be reliably interpreted.

To check the influence of random noise, we have performed the checkerboard tests for three cases of average noise deviations, 0.1 s, 0.2 s, and 0.5 s, that perturbed both *P* and *S* data. However, we present only the results for the anisotropic *P* model, as representing the major interest for us. The inversion results presented in Figure 12 show that even for an overestimated noise of 0.5 s, the main isotropic and anisotropic patterns are correctly reconstructed. It ensures that the picking errors, which might be presented in the initial catalogues, do not affect significantly the inversion results.

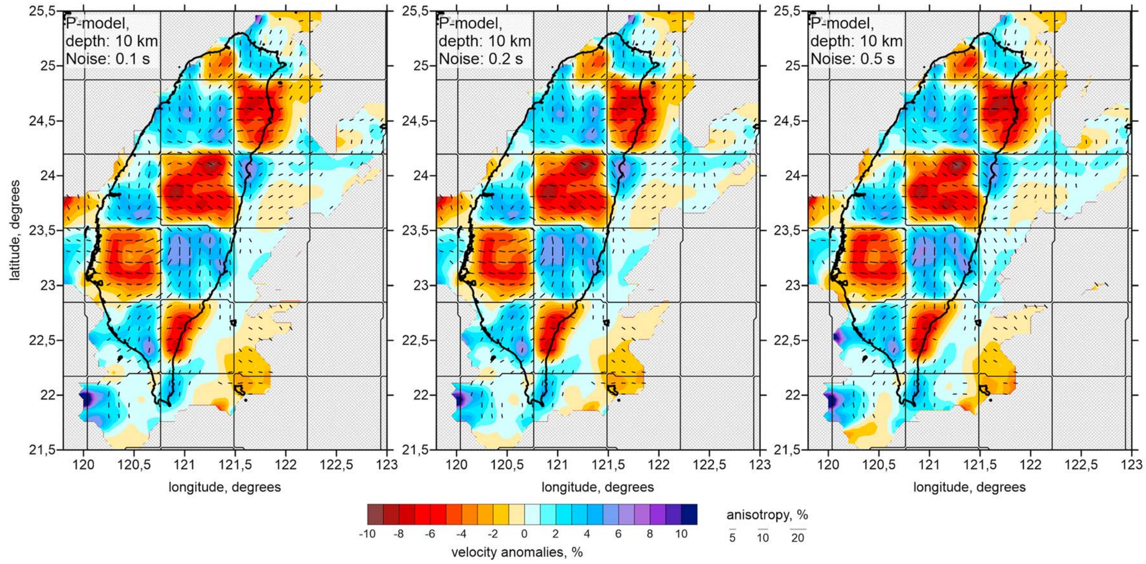


**Figure 12.** Checkerboard test for the anisotropic *P* wave velocity model reconstructed with three different noise levels: 0.1 s, 0.2 s, and 0.5 s. The shapes of synthetic anomalies are same as in the model presented in Figure 9 (left column).

## 4. Discussion of the Anisotropic Tomography Model

The main results of this study, anisotropic *P* and isotropic *S* velocity models, are presented in Figures 4 and 5 in depth sections corresponding to the crust and uppermost mantle, along with the major geological structures. In general, the resulting anisotropic patterns are consistent with a recent anisotropic model by *Huang et al*. [2015] derived from the analysis of ambient noise. In both studies, we observe the change of the anisotropy orientation from coast parallel in the shallow part to coast perpendicular in deeper sections. The consistence of these two completely independent models gives the confidence to these results. At the same time, there are some differences in details that can be explained by different resolution capacities of two methods used in these studies.

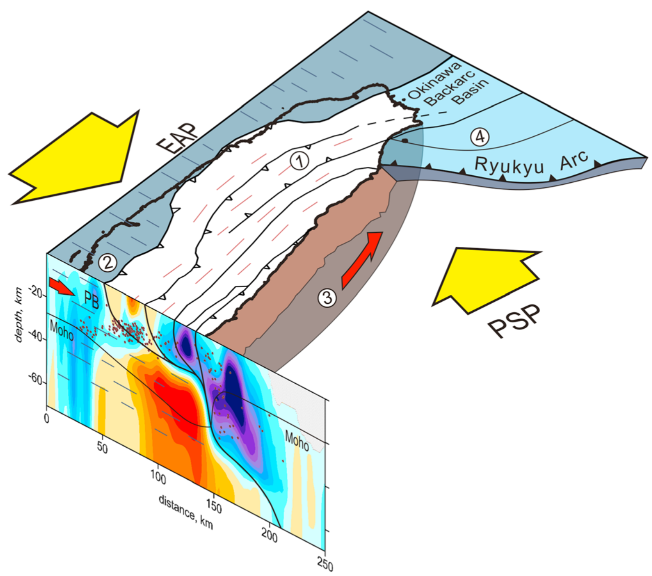


**Figure 13.** Scheme for explaining the origin of azimuthal anisotropy in the crust and uppermost mantle beneath Taiwan. The yellow arrows indicate the general orientation of plate movements; the red arrows show the possible displacements causing anisotropy beneath the eastern coast of Taiwan; the blue and red bars are the schematic orientations of anisotropy in the upper crust in the Eurasian Plate (EAP) and Taiwan. PSP is the Philippine Sea Plate, and PB is the Peikang Block. Numbers indicate the areas discussed in the text. Tomography image corresponds to *P* velocity anomalies in section 4 (Figure 4).

*Huang et al*. [2015] explain the switch of the anisotropy orientation with depth by independent deformation mechanisms in the upper and lower crust. They propose that the upper crust is mostly controlled by collision-related compressional stresses, whereas in the lower crust, the trench-perpendicular anisotropy is presumed to be caused by sinking the Eurasian lithosphere leading to shear stresses. Our model does not contradict this interpretation but provides some new features allowing us to specify the general scenario.

Our interpretation of the anisotropy patterns is schematically presented in Figure 13. The isotropic part, which is presented as colored anomalies with respect to the 1-D reference model, is generally consistent with models previously obtained by other authors [e.g., *Wu et al.*, 2007; *Kuo-Chen et al.*, 2012; *Huang et al.*, 2014a, 2014b]. The novel feature of this study is imaging the azimuthal anisotropy in Taiwan and the surrounding areas, shown in Figure 3 as bars.

In Figures 3 and 4, sections at 10 km depth show a clear correlation between the isotropic *P* and *S* anomalies and the geological manifestations on the surface. Most of the eastern part of Taiwan, including the Central Mountain Range, Longitudinal Valley, and Coastal Range (Figure 1b), is associated with high-velocity anomalies. The Coastal Range originated from the accretion of the Luzon volcanic arc following collision in Taiwan [e.g., *Suppe*, 1984; *Teng*, 1990]. Although this region was affected by recent collisional processes, it is characterized by high-velocity anomalies at shallow depths, which revealed its igneous origin.

The Central Mountain Range was a part of the Eurasian continental margin, and the Longitudinal Valley corresponds to a suture zone including fore-arc basin remnants [e.g., *Suppe*, 1984]. During the recent collision episodes, the rocks in these structures were strongly metamorphized, and therefore, they are also revealed as higher-velocity seismic anomalies compared to unconsolidated sedimentary rocks in western Taiwan.

The anisotropy results in the shallower section in areas indicated with “1” show that the orientations of most geological structures in the central and eastern parts of Taiwan almost perfectly correlate with the fast velocity directions. Similar anisotropy orientations were obtained in other studies of upper crust anisotropy in Taiwan [e.g., *Chang et al.*, 2009; *Huang et al.*, 2015; *Kuo-Chen et al.*, 2013]. This can be explained by the highly penetrative cleavage or schistosity oriented parallel to the main structural grain and thrusts, which strongly affect the anisotropic properties of rocks in the upper crust.

Along the western foothills, a belt of Neogene deposits corresponds to an elongated low-velocity anomaly in our tomography model. This zone is presumed to be most affected by the compressional processes in the main deformation front separating the EAP and PSP [*Suppe*, 1984; *Teng*, 1990]. The strong fracturing of these complexes and possible fluid saturation decreases the elastic properties of the rocks. We may also interpret the shallow low-velocity anomalies in western Taiwan as a presence of thick unconsolidated sedimentary cover. However, our seismic tomography scheme does not have sufficient vertical resolution to distinguish sediments from upper crust features. The belt in western Taiwan appears to be inhomogeneous, which explains the patchy configuration of low-velocity anomalies in the shallower section, especially for the *S* model. The anisotropy directions are mostly latitudinally oriented and follow the main structures in the western foothills area. At the same time, there are some deviations from this trend, indicating complex tectonic processes in this area that disturb the general orientation of anisotropy.

The westernmost part of Taiwan indicated with “2,” which corresponds to the margin of the EAP, is associated with a high-velocity anomaly. The orientation of the anisotropy here is perpendicular to the main trend observed in most other parts of Taiwan. This feature is novel in respect to the *Huang et al*. [2015] and other previous anisotropic models. There are several reasons for higher velocities in this area, which is known as Peikang High in the Coastal Plain. The higher velocities may indicate not only the rigid properties of the rocks in this segment but also the different compositional properties. Partly, the relatively higher velocities may be due to the fact that this domain of the Chinese margin has not been thinned during rifting and therefore is not covered by low velocities synrift/synconvergence sediments [*Lin et al*., 2003; *Mouthereau et al*., 2002]. This may also explain why the Peikang High preserves oblique anisotropy and structural fabrics inherited from former, prerifting, tectonic events. As proposed in Figure 10, this longitudinally oriented anisotropy may represent relict structures in the crust of the EAP at the Taiwan Strait, which is thought to be rigid and to have been undeformed during recent collision episodes.

In the deeper sections at 30 to 40 km depth, the isotropic anomalies show a clear separation between the low-velocity crust beneath the central part of Taiwan and the high-velocity patterns beneath the eastern coast of Taiwan and offshore areas of PSP. This highly contrasted transition may represent the boundary between the continental and oceanic crust. Note that according to this interpretation, the oceanic crust can be observed onshore beneath a narrow coastal area (up to 20 km width). The same structure was identified in previous tomography studies [e.g., *Wu et al*., 2007; *Kuo-Chen et al*., 2012; *Huang et al*., 2014a, 2014b].

To the western side of Taiwan, a similar transition from lower velocity onshore to higher-velocity offshore areas also exists, but it appears to be more dispersed compared to the eastern coast. This difference can be explained by the less contrasting properties of the crust in Taiwan and the EAP compared to the strong differences between the crust in Taiwan and the PSP.

In Figures 7 and 8, we present absolute velocities which give an idea about thickness variations of some crustal layers. In our opinion, yellow contour areas representing velocity values $V_p = 7.4$ km/s and $V_s = 4.3$ km/s may reflect variations of the Moho depth beneath Taiwan. For example, in section 4, we see that beneath eastern margin of Taiwan, the depth of this layer abruptly change from 40 km to ~25 km depth. In other sections, the variations of crustal thickness appear to be less prominent but remain significant to distinguish the continental type of the crust in the collision areas of Taiwan. Estimates for the crustal thickness variations were previously obtained in other studies based on seismic tomography [*Ustaszewski et al*., 2012], deep seismic sounding [*Yeh et al*., 1998; *McIntosh et al*., 2005], and receiver function [*Wang et al*., 2010]. Qualitatively, they provide similar features; however, the details of the Moho variations appear to be different, especially in the areas of eastern margin of Taiwan. As proposed in some of these studies, beneath these areas, the crust of the eastern Taiwan underthrusts underneath the Philippine Sea Plate. Therefore, several Moho solutions corresponding to the upper and lower plates are possible.

The anisotropy patterns at 40 km depth beneath Taiwan appear to be different from those observed at 10 km depth. We observe strong coast-perpendicular anisotropy in the central part of the island in area indicated with 2. This observation is consistent with a previous study by *Chen et al*. [2003] who presented an anisotropy map beneath Taiwan based on the analysis of *Pn* traveltimes. Same orientations of anisotropy are reported by *Huang et al*. [2015] based on the ambient noise analysis. In other parts of Taiwan, our model demonstrates strongly variable orientations for the anisotropy. In *Chen et al*.'s [2003] model, the anisotropy directions in these areas are also strongly scattered but are not always consistent with our model. The difference might be related to the different depth resolutions of the anisotropy parameters, which appear to vary strongly with depth.

We propose that this coast-perpendicular anisotropy beneath the central part of Taiwan (dotted line in Figure 4) might represent a part of the Peikang Block with coast-perpendicular anisotropic properties propagating underneath Taiwan. The W-E anisotropy in of the Peikang Block may represent the crustal and mantle lithosphere fabric originated from preorogenic tectonic processes in the Eurasian Plate margins. When considering the horizontal sections in Figure 4 from up to down, this zone appear to expand toward the eastern coast of Taiwan. We propose that this feature represents the eastward underthrusting of a rigid fragment of the Eurasian Plate, as schematically shown in Figure 13. In turn, this underthrusting may trigger the initiation of a subduction zone with the nearly opposite direction in respect to the Ryukyu arc, and it might be connected with the Luzon arc to the SE of Taiwan. Alternatively, orogen-perpendicular anisotropy at 40 km and deeper may be caused by asthenospheric flows below the crust. However, without using additional information, the tomography cannot distinguish mantle flows from the lithospheric fabrics.

At 30 and 40 km depth, in areas along easternmost Taiwan indicated with "3," the fast *P* velocity directions follow the coast from the southern edge to the junction with the Ryukyu trench. This pattern may be explained by strong variations in the crustal thickness, which cause a type of a vertical step in the Moho interface beneath the eastern coast. Due to the oblique movement of the PSP, this step should be associated with contrasting laterally oriented displacements, as shown in Figure 13 by a red arrow, which may cause significant seismic anisotropy.

In the northeastern part of Taiwan Island and in the offshore areas marked with "4," we observe a series of low-velocity patterns at 10 km depth (Figure 4), which might be associated with the accretion zone of the Ryukyu arc (Nanao Basin). The anisotropy orientations form a circular structure that almost perfectly follows the configuration of the Ryukyu trench. This anisotropy is a clear indicator of deformations in the accretion zone, which may lead to the formation of linear structures in the Nanao Basin. At 40 km depth, we observe a high-velocity anomaly that may represent the subducting Philippine Sea Plate. As in the shallower sections, the anisotropy patterns follow the curvature of the Ryukyu trench, indicating the dominant trench-parallel orientations of the structures.

## 5. Conclusions

In this study, we benefit from a comprehensive data set from Taiwan and the latest version of the passive source anisotropic tomography code ANITA. The three-dimensional anisotropic *P* and isotropic *S* wave velocity structures in the Taiwan region are determined. This is a first 3-D anisotropic model of the crust and uppermost mantle Taiwan derived from the inversion of traveltime data from regional earthquakes. It appears to be consistent with most determinations of anisotropy for the same region obtained using different approaches and data, such as ambient noise, shear wave splitting, active source data analysis, and *Pn* traveltimes (2-D model below Moho). This gives higher confidence to the distributions of anisotropy and supports their geodynamic interpretation. At the same time, our model reveals some important features in the distributions of velocity anomalies and anisotropy that allow us proposing new geodynamic scenario related to the development of the Taiwan orogeny.

The results show that the anisotropy directions are parallel with geological structures in the central and eastern parts of Taiwan at depths less than 20 km. However, the *P* velocities change from high to low anomalies in the Central Range region for depths greater than 20 km. The anisotropy directions also change to perpendicular for the geological structures in the southern part of the Central Range. In other regions, the anisotropy directions are generally parallel to tectonic structures. Strong anisotropy in the Taiwan region is found in this study. The anisotropic velocity model can reduce the *P* wave traveltime residual 16% more than isotropic model, which shows that anisotropic properties should be taken into account during tomography inversion in the future, especially in plate convergence zones such as Taiwan.

Based on the anisotropic inversion results, we conclude that there is a zone of strong coast-perpendicular displacements beneath central Taiwan below the Moho interface that were possibly caused by eastward underthrusting of a rigid fragment of the Peikang Block belonging to the Eurasian Plate. The strong anisotropy along the eastern coast of Taiwan is probably due to mantle displacements that were induced by oblique movement of the PSP and step-shaped contrasts between the thick crust in Taiwan and the thin crust in the PSP.

**Acknowledgments**
We are grateful to Frederic Mouthereau and to the anonymous Associate Editor and reviewer for rigorous criticism that helped us to improve the content of the paper. This study is supported by the Joint Research Project of the Siberian Branch of RAS and the National Science Council of Taiwan. Ivan Koulakov is supported by RNSF grant 14-17-00430. The authors extend their appreciation to the Deanship of Scientific Research at King Saud University for funding the work through the research group project RG-1435-027. The data for this study are provided by the Taiwan Central Weather Bureau Seismic Network (CWBSN), Japan Meteorological Agency (JMA), and National Central University (NCU).

## References

Anglin, D. K., and M. J. Fouch (2005), Seismic anisotropy in the Izu-Bonin subduction system, *Geophys. Res. Lett.*, *32*, L09307, doi:10.1029/2005GL022714.

Audoine, E., M. K. Savage, and K. Gledhill (2004), Anisotropic structure under a back arc spreading region, the Taupo Volcanic Zone, New Zealand, *J. Geophys. Res.*, *109*, B11305, doi:10.1029/2003JB002932.

Chang, E. T., W. T. Liang, and Y. B. Tsai (2009), Seismic shear wave splitting in upper crust characterized by Taiwan tectonic convergence, *Geophys. J. Int.*, *177*(3), 1256–1264, doi:10.1111/j.1365-246X.2009.04110.x.

Chen, C. H., Y. H. Chen, H. Y. Yen, and G. K. Yu (2003), Lateral variations of *Pn* velocity and anisotropy in Taiwan from travel-time tomography, *Earth Planets Space*, *55*, 223–230.

Hearn, T. M. (1996), Anisotropic *Pn* tomography in the western United States, *J. Geophys. Res.*, *101*(B4), 8403–8414.

Hsu, S. K. (2001), Subduction/collision complexities in the Taiwan-Ryukyu junction area: Tectonics of the northwestern corner of the Philippine Sea Plate, *J. Terr. Atmos. Ocean Sci.*, *12*, 209–230.

Huang, B. S., W. G. Huang, W. T. Liang, R. J. Rau, and N. Hirata (2006), Anisotropy beneath an active collision orogen of Taiwan: Results from across islands array observations, *Geophys. Res. Lett.*, *33*, L24302, doi:10.1029/2006GL027844.

Huang, H. H., Y. M. Wu, X. D. Song, C. H. Chang, S. J. Lee, T. M. Chang, and H. H. Hsieh (2014a), Joint *Vp* and *Vs* tomography of Taiwan: Implications for subduction-collision orogeny, *Earth Planet. Sci. Lett.*, *392*, 177–191, doi:10.1016/j.epsl.2014.02.026.

Huang, H. H., Y. M. Wu, X. D. Song, C. H. Chang, and H. Kuo-Chen (2014b), Investigating lithospheric velocity structures beneath Taiwan region by nonlinear joint inversion of local and teleseismic *P* wave data: Slab continuity and deflection, *Geophys. Res. Lett.*, *41*, 6350–6357, doi:10.1002/2014GL061115.

Huang, T. Y., Y. Gung, W. T. Liang, L. Y. Chiao, and L. S. Teng (2012), Broad-band Rayleigh wave tomography of Taiwan and its implications on gravity anomalies, *Geophys. Res. Lett.*, *39*, L05305, doi:10.1029/2011GL050727.

Huang, T. Y., Y. Gung, B. Y. Kuo, L. Y. Chiao, and Y. N. Chen (2015), Layered deformation in the Taiwan orogen, *Science*, *349*(6249), 720–723.

Hwang, R. D., and G. K. Yu (2005), Shear-wave velocity structure of upper mantle under Taiwan from the array analysis of surface waves, *Geophys. Res. Lett.*, *32*, L07310, doi:10.1029/2004GL021868.

Kim, K. H., J. M. Chiu, J. Pujol, K. C. Chen, B. S. Huang, Y. H. Yeh, and P. Shen (2005), Three-dimensional $V_p$ and $V_s$ structural model associated with the active subduction and collision tectonics in the Taiwan region, *Geophys. J. Int.*, *162*, 204–220, doi:10.1111/j.1365-246X.2005.02657.x.

Koulakov, I. (2009a), Out-of-network events can be of great importance for improving results of local earthquake tomography, *Bull. Seismol. Soc. Am.*, *99*(4), 2556–2563, doi:10.1785/0120080365.

Koulakov, I. (2009b), LOTOS code for local earthquake tomographic inversion: Benchmarks for testing tomographic algorithms, *Bull. Seismol. Soc. Am.*, *99*(1), 194–214, doi:10.1785/0120080013.

Koulakov, I., and S. V. Sobolev (2006), Moho depth and three-dimensional *P* and *S* structure of the crust and uppermost mantle in the Eastern Mediterranean and Middle East derived from tomographic inversion of local ISC data, *Geophys. J. Int.*, *164*(1), 218–235, doi:10.1111/j.1365-246X.2005.02791.x.

Koulakov, I., A. Jakovlev, and B. G. Luehr (2009), Anisotropic structure beneath central Java from local earthquake tomography, *Geochem. Geophys. Geosyst.*, *10* Q02011, doi:10.1029/2008GC002109.

Koulakov, I., Y.-M. Wu, H.-H. Huang, N. Dobretsov, A. Jakovlev, I. Zabelina, K. Jaxybulatov, and V. Chervov (2014), Slab interactions in the Taiwan region based on the *P*- and *S*-velocity distributions in the upper mantle, *J. Asian Earth Sci.*, *79*, Part A, 53–64, doi:10.1016/j.jseaes.2013.09.026.

Koulakov, I., E. Kukarina, I. H. Fathi, S. El Khrepy, and N. Al-Arifi (2015), Anisotropic tomography of Hokkaido reveals delamination-induced flow above a subducting slab, *J. Geophys. Res. Solid Earth*, *120*, 3219–3239, doi:10.1002/2014JB011823.

Ku, C.-Y., and S.-K. Hsu (2009), Crustal structure and deformation at the northern Manila Trench between Taiwan and Luzon islands, *Tectonophysics*, *466*, 229–240, doi:10.1016/j.tecto.2007.11.012.

Kuo-Chen, H., F. T. Wu, and S. W. Roecker (2012), Three-dimensional P velocity structures of the lithosphere beneath Taiwan from the analysis of TAIGER and Related seismic datasets, *J. Geophys. Res.*, *117*, B06306, doi:10.1029/2011JB009108.

Kuo-Chen, H., P. Środa, F. Wu, C. Y. Wang, and Y. W. Kuo (2013), Seismic anisotropy of the upper crust in the mountain ranges of Taiwan from the TAIGER explosion experiment, *Terr. Atmos. Ocean. Sci.*, *24*, 963–970, doi:10.3319/TAO.2013.07.30.01(T).

Levin, V., D. Droznin, J. Park, and E. Gordeev (2004), Detailed mapping of seismic anisotropy with local shear waves in southeastern Kamchatka, *Geophys. J. Int.*, *158*, 1009–1023, doi:10.1111/j.1365-246X.2004.02352.x.

Lin, A. T., A. B. Watts, and S. P. Hesselbo (2003), Cenozoic stratigraphy and subsidence history of the South China Sea margin in the Taiwan region, *Basin Res.*, *15*(4), 453–478.

Lin, J. Y., J. C. Sibuet, C. S. Lee, S. K. Hsu, and F. Klingelhoefer (2007), Origin of the southern Okinawa Trough volcanism from detailed seismic tomography, *J. Geophys. Res.*, *112*, B08308, doi:10.1029/2006JB004703.

Long, M. D. (2013), Constraints on subduction geodynamics from seismic anisotropy, *Rev. Geophys.*, *51*, 76–112, doi:10.1002/rog.20008.

Long, M. D., and R. D. Van Der Hilst (2006), Shear wave splitting from local events beneath the Ryukyu arc: Trench-parallel anisotropy in the mantle wedge, *Phys. Earth Planet. Inter.*, *155*, 300–312, doi:10.1016/j.pepi.2006.01.003.

McIntosh, K., Y. Nakamura, T.-K. Wang, R.-C. Shih, A. Chen, and C.-S. Liu (2005), Crustal-scale seismic profiles across Taiwan and the western Philippine Sea, *Tectonophysics*, *401*, 23–54.

Mouthereau, F., B. Deffontaines, O. Lacombe, and J. Angelier (2002), Variations along the strike of the Taiwan thrust belt: Basement control on structural style, wedge geometry, and kinematics, *Geol. Soc. Am. Spec. Pap.*, *358*, 35–58.

Nolet, G. (1987), Seismic wave propagation and seismic tomography, in *Seismic Tomography*, edited by G. Nolet, pp. 1–23, Reidel, Dordrecht, Netherlands.

Paige, C. C., and M. A. Saunders (1982), LSQR: An algorithm for sparse linear equations and sparse least squares, *ACM Trans. Math. Software*, *8*, 43–71.

Rabbel, W., I. Koulakov, A. N. Dinc, and A. Jakovlev (2011), Arc-parallel shear deformation and escape flow in the mantle wedge of the Central America subduction zone: Evidence from *P* wave anisotropy, *Geochem. Geophys. Geosyst.*, *12*, Q05S31, doi:10.1029/2010GC003325.

Rau, R. J., W. T. Liang, H. Kao, and B. S. Huang (2000), Shear wave anisotropy beneath the Taiwan orogeny, *Earth Planet. Sci. Lett.*, *177*(3), 177–192, doi:10.1016/S0012-821X(00)00058-3.

Suppe, J. (1984), Kinematics of arc-continent collision, flipping of subduction, and backarc spreading near Taiwan, *Mem. Geol. Soc. China*, *6*, 21–33.

Teng, L. S. (1990), Geotectonic evolution of late Cenozoic arc-continent collision in Taiwan, *Tectonophysics*, *183*, 57–76, doi:10.1016/0040-1951(90)90188-E.

Ustaszewski, K., Y. M. Wu, J. Suppe, H. H. Huang, C. H. Chang, and S. Carena (2012), Crust-mantle boundaries in the Taiwan-Luzon arc-continent collision system determined from local earthquake tomography and 1D models: Implications for the mode of subduction polarity reversal, *Tectonophysics*, *578*, 31–49, doi:10.1016/j.tecto.2011.12.029.

Wang, H. L., L. Zhu, and W. Chen (2010), Moho depth variation in Taiwan from teleseismic receiver functions, *J. Asian Earth Sci.*, *37*(3), 286–291.

Wang, Z., D. Zhao, J. Wang, and H. Kao (2006), Tomographic evidence for the Eurasian lithosphere subducting beneath south Taiwan, *Geophys. Res. Lett.*, *33*, L18306, doi:10.1029/2006GL027166.

Wu, F. T., R.-J. Rau, and D. Salzberg (1997), Taiwan orogeny: Thin-skinned or lithospheric collision?, *Tectonophysics*, *274*, 191–220, doi:10.1016/S0040-1951(96)00304-6.

Wu, Y. M., C. H. Chang, L. Zhao, T. L. Teng, and M. Nakamura (2008), A comprehensive relocation of earthquakes in Taiwan from 1991 to 2005, *Bull. Seismol. Soc. Am.*, *98*, 1471–1481, doi:10.1785/0120070166.

Wu, Y. M., J. B. H. Shyu, C. H. Chang, L. Zhao, M. Nakamura, and S. K. Hsu (2009), Improved seismic tomography offshore northeastern Taiwan: Implications for subduction and collision processes between Taiwan and the southernmost Ryukyu, *Geophys. J. Int.*, *178*, 1042–1054, doi:10.1111/j.1365-246X.2009.04180.x.

Wu, Y.-M., C.-H. Chang, L. Zhao, J. B. H. Shyu, Y.-G. Chen, K. Sieh, and J.-P. Avouac (2007), Seismic tomography of Taiwan: Improved constraints from a dense network of strong motion stations, *J. Geophys. Res.*, *112*, B08312, doi:10.1029/2007JB004983.

Yang, X., K. M. Fischer, and G. Abers (1995), Seismic anisotropy beneath the Shumagin Islands segment of the Aleutian–Alaska subduction zone, *J. Geophys. Res.*, *100*(B9), 18,165–18,177, doi:10.1029/95JB01425.

Yeh, Y. H., et al. (1998), Onshore/offshore wide-angle deep seismic profiling in Taiwan, *Terr. Atmos. Oceanic Sci.*, *9*, 301–316.

You, S. H., Y. Gung, L. Y. Chiao, Y. N. Chen, C. H. Lin, W. T. Liang, and Y. L. Chen (2010), Multiscale ambient noise tomography of short-period Rayleigh waves across northern Taiwan, *Bull. Seismol. Soc. Am.*, *100*(6), 3165–3173, doi:10.1785/0120090394.